Proceedings of the ASME 2010 3rd Joint US-European Fluids Engineering Summer Meeting and 8th International Conference on Nanochannels, Microchannels, and Minichannels
FEDSM-ICNMM2010
August 1-5, 2010, Montreal, Canada

FEDSM-ICNMM2010-30663

NUMERICAL SIMULATION OF RIVULET DYNAMICS ASSOCIATED WITH RAIN-WIND INDUCED VIBRATION.

Ian J. Taylor
Dept. of Mechanical Engineering, University of Strathclyde
Glasgow, UK

Andrew C. Robertson
Doosan Babcock
Porterfield Road, Renfrew, UK

ABSTRACT

On wet and windy days, the inclined cables of cable-stayed bridges can experience large amplitude, potentially damaging oscillations known as Rain-Wind Induced Vibration (RWIV). The phenomenon is believed to be the result of a complicated nonlinear interaction between rivulets of rain water that run down the cables and the wind loading on the cables due to the unsteady aerodynamic flow field. A numerical method has been developed at the University of Strathclyde, to simulate aspects of RWIV, the results of which can be used to assess the importance of the water rivulets on the instability. This combines a Discrete Vortex Method solver to determine the external flow field and unsteady aerodynamic loading and a pseudo-spectral solver based on lubrication theory to model the water on the surface of the body and which is used to determine the evolution and growth of the water rivulets under external loading. These two models are coupled to simulate the interaction between the aerodynamic field and the thin liquid film on a horizontal circular cylinder. The results illustrate the effects of various loading combinations, and importantly demonstrate rivulet formation in the range of angles previous research has indicated that these may suppress the Karman vortex and lead to a galloping instability. These rivulets are found to be of self limiting thickness in all cases

INTRODUCTION

Rain-Wind Induced Vibration (RWIV) is now accepted as a distinct aeroelastic phenomenon that can occur on the inclined cables of cable-stayed bridges. Typically RWIV involves large amplitude oscillations and is thought to occur due to the three way interaction between unsteady aerodynamic loading, rivulets of rain water running down the surface of the cable and the structural dynamics of the cable. The phenomenon was first formally reported by Hikami and Shiraishi [1] who recorded the strong influence of rain on large amplitude cable oscillations during construction of the Meikonishi Bridge, Japan. Since this initial event, there have been numerous reported observations and investigations of RWIV on cable-stayed bridges.

RWIV has been the subject of a large amount of international research activity, utilizing a range of techniques, in an attempt to gain a satisfactory understanding of this instability. To date there have been numerous full scale investigations of RWIV events on bridges [2] and a range of wind tunnel experiments to ascertain particular aspects of the phenomenon [3-8]. Despite this research effort, a full understanding of the aeroelastic phenomenon has yet to be obtained due to the complexity of the interaction between the rivulets, the aerodynamic flow field, and the cable dynamics.

In summary, the data obtained thus far from various researchers has determined a range of conditions under which the phenomenon is most likely to occur. These include wind speeds of between 5 and 15 m/s, corresponding to Reynolds numbers between 50×10^3 to 1.5×10^5 and reduced velocities $20 \leq U_R \leq 90$ [5], where Re is based on the wind speed normal to the cable, U_∞, and the cable diameter, and U_R is defined by $U_R = U_\infty/fD$. Moderate rainfall is required [1] though it is difficult to ascertain a consistent definition of "moderate" rain from the published research, or even water flow rates from experiments. Also, on a number of occasions, vibrations have been identified as RWIV despite having been observed in dry conditions. It is postulated that due to differences in the conditions that these are a result of a different but related physical phenomenon, such as vortex induced vibration at high reduced velocity [3].

Using the angles of inclination in the cable pylon plane, α, and yaw angle, β, as displayed in the configuration of stay cable geometry in Fig. 1, it can be said that RWIV typically occurs in cables which descend in the windward direction, at yaw angles between $20° \leq \beta \leq 60°$ [5, 9], and at angles of inclination between $20° \leq \alpha \leq 45°$ [1, 10]. The cables which undergo

vibration are typically found to fall within the diameter range 100mm ≤ D ≤ 250mm [5] and to have low structural damping, with the damping ratio typically $\zeta \leq 0.5\%$ [8]. The response has been found to be in the 0.6 to 3 Hz frequency range [1, 11], to occur in more than one mode [2] and to vibrate at an angle aligned to the cable-pylon plane (Fig. 1). The magnitude of this vibration, although amplitude limited, is significant with peak to peak responses of up to 2 m being reported [11].

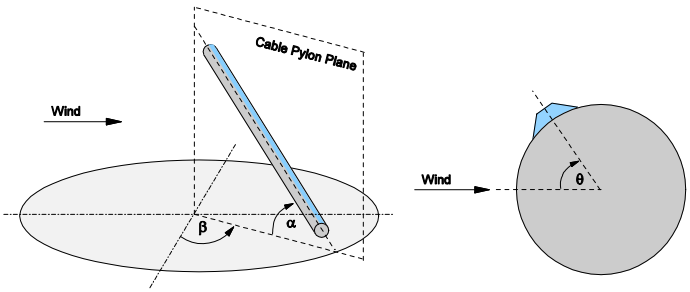

FIGURE 1: DEFINITION OF ORIENTATION OF STAY CABLE SYSTEM GEOMETRY.

One of the key aspects of the RWIV instability is the presence and location of the rivulets of rain water on the surface of the cable. In experiments, it has been observed and is now generally accepted, that under most conditions causing RWIV, that the thin film of rain water present on the cable normally accumulates to form two rivulets, one on the upper leeward side and one on the lower windward side, and that the former is largely responsible for the vibration [7, 9]. Other studies have concentrated on specific aspects of the location and dynamics of the rivulet motion, to identify the effect of the rivulets on the external aerodynamic field and vice versa. The latter investigations can be broadly separated into two distinct classes, namely those where the rivulet is replaced by a fixed, static, rigid protuberance, i.e. an 'artificial rivulet' [7] and those where a film of water is sprayed onto the surface of the cable and the rivulets are allowed to form 'naturally' [4-6, 8, 9]. Both classes indicate that the presence of the rivulet on the upper surface is largely responsible for the vibration. The latter class also indicates that when free to do so, the rivulets oscillate circumferentially at the same frequency as that with which the cable vibrates. Differentiating between the effect of circumferential oscillation and rivulet position in the 'artificial rivulet' investigations has, however, proven more difficult and led to discrepancies in the literature. In particular Verwiebe and Ruscheweyh [6] determined that the circumferential oscillation of the rivulet is a primary cause of RWIV, whereas Bosdogianni and Olivari [7] suggest that the rivulet location, not its profile or circumferential oscillation, initiates the response.

Despite all of this research effort, however, computational models for RWIV are scarce due to the complexity of the problem and the need to couple models for the thin film of rain water, the unsteady aerodynamic field, and the structural dynamics of the cable. To date, the majority of the numerical investigations of RWIV have focused on fixed rigid artificial rivulets, with 2D and 3D large eddy simulations (LES) examining the effect that static rivulets have on the overall flow field [12]. Lemaitre et al [13] however presented a different approach using lubrication theory and the time averaged flow-field over a circular cylinder to ascertain the evolution of the rain water rivulets.

Research in the Department of Mechanical Engineering at the University of Strathclyde has focused on developing a numerical model to investigate aspects of RWIV. The approach adopted is to couple a modified pre-existing unsteady aerodynamic solver for the external aerodynamic flow field with a solver based on a thin-film model for the evolution and deformation of the water rivulets. The development of the thin-film model for the rivulets, and the results from the validation of the method are presented in detail in [14], with results from the unsteady aerodynamic solver summarized in [15, 16].

The research presented herein summarizes the development of a coupled method, where the unsteady aerodynamic field determines the evolutionary response of the rivulets, which in turn modifies the aerodynamics due to the change in effective shape of the body. Results for various loading configurations are summarized, along with key findings in relation to the underlying mechanism for RWIV. It is thought that this novel numerical approach provides the most advanced model to date for assessing the RWIV instability.

AERODYNAMIC MODEL

The two-dimensional discrete vortex method used for this analysis is a modified version of the DIVEX code developed at the Universities of Strathclyde and Glasgow [17, 18]. DIVEX has previously proven successful with unsteady, incompressible, highly separated flows such as those under investigation and for related problems involving other aeroelastic phenomenon [17, 18], which were examined in an earlier stage of development. For the RWIV phenomenon, an extensive investigation into the effects of artificial rivulets on the unsteady aerodynamic flow field, has been successfully undertaken, with the results highlighting the importance of the rivulet location on the cylinder surface that in certain configurations, may lead to a galloping instability [15].

The numerical technique utilised by vortex methods is based on the discretisation of the vorticity field rather than the velocity field, into a series of vortex particles [16, 17]. These particles, of finite core size, each carry a certain amount of circulation, and are tracked throughout the flow field they collectively induce. As such, the model does not require a calculation mesh providing a very different approach to more traditional grid based computational fluid dynamics methods. One of the main advantages of such vortex methods over grid based approaches, however, is that their Lagrangian nature significantly reduces some of the problems associated with grid methods, such as numerical diffusion and difficulties in achieving resolution of small scale vortical structures in the flow. Vortex particles are naturally concentrated into areas of non-zero vorticity and enable vortex methods to capture these small scale flow structures in more detail. This aspect of the numerical approach make it ideally suited to analyse the effects of artificial rivulets both locally and on the overall flow field.

Mathematical Formulation

Two dimensional incompressible viscous flow is governed by the vorticity-stream function form of the continuity and Navier-Stokes Eqs. (1) and (2) :

Continuity Equation :

$$\nabla^2 \Psi = -\omega \tag{1}$$

Vorticity transport Equation :

$$\frac{\partial \vec{\boldsymbol{\omega}}}{\partial t} + \left(\vec{\mathbf{U}}.\nabla\right)\vec{\boldsymbol{\omega}} = \nu \nabla^2 \vec{\boldsymbol{\omega}} \tag{2}$$

where the vorticity, $\vec{\boldsymbol{\omega}}$, is defined as the curl of the velocity (3) and $\vec{\boldsymbol{\Psi}}$ is a vector potential defined by (4)

$$\vec{\boldsymbol{\omega}} = \nabla \times \vec{\mathbf{U}} \qquad \text{with} \quad \vec{\boldsymbol{\omega}} = \vec{\mathbf{k}}\omega \tag{3}$$

$$\vec{\mathbf{U}} = \nabla \times \vec{\boldsymbol{\Psi}}, \quad \nabla.\vec{\boldsymbol{\Psi}} = 0, \quad \text{and} \quad \vec{\boldsymbol{\Psi}} = \vec{\mathbf{k}}\Psi \tag{4}$$

The vorticity transport Eq. (2) defines the motion of vorticity in the flow due to convection and diffusion. As the pressure field is not explicitly defined in (2), the variation of vorticity at a point in the flow is therefore influenced by the surrounding flow velocity and vorticity.

The calculations are subject to the far field boundary conditions (5) and the no-slip and no-penetration conditions at the surface of the body (6).

$$\vec{\mathbf{U}} = \vec{\mathbf{U}}_\infty \quad \text{or} \quad \nabla\Psi = \nabla\Psi_\infty \quad \text{on} \quad S_\infty \tag{5}$$

$$\vec{\mathbf{U}} = \vec{\mathbf{U}}_i \quad \text{or} \quad \nabla\Psi = \nabla\Psi_i \quad \text{on} \quad S_i \tag{6}$$

Proper definition of the problem allows for only one of the normal and tangential boundary conditions at the body surface to be explicitly applied. In the current formulation, this is the normal component, no-penetration condition. However, the tangential, no-slip condition is implicitly satisfied due to the representation of the internal kinematics of each solid body. The velocity at a point $\vec{r}$ on the surface or within body i being described by :

$$\vec{\mathbf{U}}_i = \vec{\mathbf{U}}_{ic} + \vec{\boldsymbol{\Omega}}_i \times \left(\vec{\mathbf{r}}_p - \vec{\mathbf{r}}_{ic}\right) \tag{7}$$

where $\vec{\mathbf{r}}_{ic}$ is a fixed reference point on the body. This may also be represented in stream function form

$$\nabla^2 \Psi_i = -2\Omega_i \qquad \text{in } B_i \tag{8}$$

The relationship between the velocity and the vorticity is derived by the application of Green's Theorem to (1) for the flow region, F, and to (8) for the body region, B_i, combined through the boundary conditions (5) and (6) [16, 17]. From this, the velocity field is calculated using the Biot-Savart law, which expresses the velocity in terms of the vorticity field. For a point p outside the solid region, the velocity is given by :

$$\vec{\mathbf{U}}_p = \vec{\mathbf{U}}_\infty + \frac{1}{2\pi}\int_F \omega \frac{\vec{\mathbf{k}} \times \left(\vec{\mathbf{r}}_p - \vec{\mathbf{r}}\right)}{\left\|\vec{\mathbf{r}}_p - \vec{\mathbf{r}}\right\|^2} dF + \int_{B_i} 2\Omega_i \frac{\vec{\mathbf{k}} \times \left(\vec{\mathbf{r}}_p - \vec{\mathbf{r}}\right)}{\left\|\vec{\mathbf{r}}_p - \vec{\mathbf{r}}\right\|^2} dB_i \tag{9}$$

The pressure distribution on the body surface can be evaluated by integrating the pressure gradient along the body contour. The pressure at node j on the body surface is given by Eq. (10)

$$\frac{1}{\rho}\frac{\partial P}{\partial s} = -\vec{\mathbf{s}}.\frac{D\vec{\mathbf{U}}_c}{Dt} - \vec{\mathbf{n}}.\left(\vec{\mathbf{r}} - \vec{\mathbf{r}}_c\right)\frac{D\Omega}{Dt} + \vec{\mathbf{s}}.\left(\vec{\mathbf{r}} - \vec{\mathbf{r}}_c\right)\Omega^2 + \nu\frac{\partial \omega}{\partial n} \tag{10}$$

where the first three terms on the RHS are due to the body motion and represent the surface tangential components of the body reference point acceleration, the rotational acceleration and the centripetal acceleration. The final term is the negative rate of vorticity creation at the body surface and is calculated from the vorticity distribution created in the control zone between time t-Δt and t [20]. The resulting pressure distribution is integrated around the body surface to calculate the aerodynamic forces on the body and the moment about the body reference point at a particular timestep.

NUMERICAL MODELLING OF WATER RIVULET

Two-dimensional, unsteady flow of a thin film of incompressible viscous fluid with uniform dynamic viscosity, μ, and density, ρ, on the outer surface of a stationary horizontal circular cylinder of radius R is considered. This restricts all loading to act purely within the two-dimensional system defined and is in line with the previous numerical and analytical studies into aspects of RWIV [10-13]. Should an inclined cylinder be considered, then the effective component of gravity would be reduced; however, this would introduce a gravity-driven flow down the cylinder, and would also introduce uncertainties regarding the effective cylinder cross-section and the resulting aerodynamic loading.

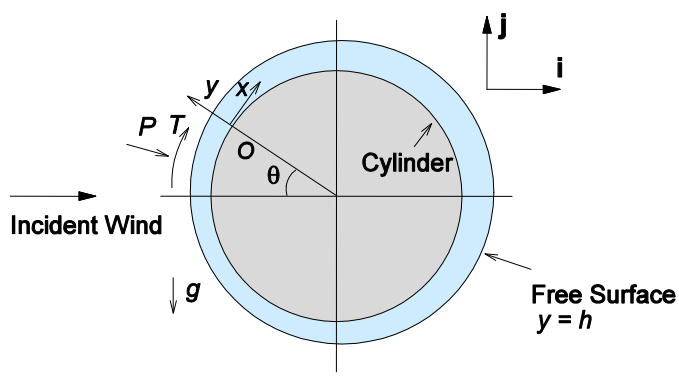

FIGURE 2: A THIN FLUID FILM ON A HORIZONTAL CYLINDER.

As Fig. 2 shows, the free surface of this film is subject to a prescribed pressure, $P = P(\theta, t)$, and a prescribed shear, $T = T(\theta, t)$, exerted by the external aerodynamic field, which are both functions of clockwise angle from the windward (left-hand) horizontal, θ (0° ≤ θ ≤ 360°) and time t.

Model Description

We take the film to be thin, with its aspect ratio ε (defined by $\varepsilon = H/R$, where H denotes a typical film thickness) satisfying $\varepsilon \ll 1$.

We denote the fluid velocity and pressure by **u** and p, respectively. Initially we refer the description to polar coordinates r, θ, z with the z axis along the axis of the cylinder; then the surface of the cylinder is given by $r = R$. We denote the film thickness by $h = h(\theta, t)$ (unknown *a priori*); then the free surface of the film is given by $r = R + h$. Near any station θ = constant we may alternatively refer the description to a local Cartesian coordinate system $Oxyz$ with Ox tangential to the cylinder (increasing in the direction of increasing θ, so that $x = R\theta$ + constant) and Oy along the outward normal to the cylinder, with y defined by $y = r - R$, so that the cylinder is at $y = 0$ and the free surface is at $y = h$. In the latter coordinate system the governing mass-conservation and Navier–Stokes equations give, at leading order in ε,

$$u_x + v_y = 0 \tag{11}$$

$$0 = -p_x - \rho g \cos\theta + \mu u_{yy} \tag{12}$$

$$0 = -p_y \tag{13}$$

where subscripts denote differentiation, and we have written

$$\mathbf{u} = u\mathbf{i} + v\mathbf{j}, \quad \mathbf{g} = -g\left(\mathbf{i}\cos\theta + \mathbf{j}\sin\theta\right) \tag{14}$$

In (12) and (13), the inertia terms have been neglected; this is valid provided that the film Reynolds number $\hat{R}e$ (defined by $\hat{R}e = \hat{U}R/\nu$, where $\nu = \mu/\rho$ and $\hat{U}$ are the kinematic viscosity and a typical velocity of the film, respectively) is such that $\varepsilon^2\hat{R}e \ll 1$. Also since the film is thin ($\varepsilon \ll 1$), terms such as u_{xx} and v_{yy} in the momentum balances are negligible, as is a contribution $\rho g \sin\theta$ in (13). Equations. (11)-(13) are subject to the no-slip and no-penetration conditions on the cylinder:

$$u = v = 0 \quad \text{on} \quad y = 0 \tag{15}$$

and, at the free surface, to the kinematic condition

$$v = h_t + uh_x \quad \text{on} \quad y = h \tag{16}$$

the tangential stress condition

$$\mu u_y = T \quad \text{on} \quad y = h \tag{17}$$

and the normal stress condition

$$p = \gamma\kappa + P \quad \text{on} \quad y = h \tag{18}$$

where γ is the coefficient of surface tension and κ is the mean curvature of the free surface, given to first order by

$$\kappa = \frac{1}{R} - \frac{1}{R^2}\left(h + h_{\theta\theta}\right) \tag{19}$$

The azimuthal volume flux of fluid in the film is given by

$$Q = \int_0^h u\, dy \tag{20}$$

and using this and (11) we may replace (16) by the local conservation law

$$h_t + Q_x = 0 \tag{21}$$

Evolution Equation For *h*(θ, *t*)

Integrating (13) subject to (18) we obtain

$$p = \gamma\kappa + P \tag{22}$$

(independent of y), and then integrating (12) with respect to y subject to (15) and (17) we obtain

$$u = -\frac{1}{2\mu}\left(\rho g\cos\theta + p_x\right)\left(2hy - y^2\right) + \frac{Ty}{\mu} \tag{23}$$

Therefore, from (20)

$$Q = -\frac{1}{3\mu}\left(\rho g\cos\theta + p_x\right)h^3 + \frac{Th^2}{\mu} \tag{24}$$

Finally, substituting (24) into (21) and using (19) and (22) leads to the evolution equation for $h(\theta, t)$:

$$h_t + \left(\frac{Th^2}{2\mu R}\right)_\theta - \left[\frac{h^3}{3\mu R}\left(\rho g\cos\theta - \frac{\gamma}{R^3}\left(h + h_{\theta\theta}\right)_\theta + \frac{P_\theta}{R}\right)\right]_\theta = 0 \tag{25}$$

This equation is to be solved subject to an initial condition of the form $h(\theta, 0) = h_0(\theta)$, where $h_0(\theta)$ is the initial thickness of the film. For definiteness in the present work we choose an initially uniform film h_0 = constant, and allow the film to evolve according to (25) to see if rivulets develop.

The present evolution equation (25) agrees with the corresponding equation given by Lemaitre et al. [13] in the case of flow over a stationary cylinder, and with an earlier equation by Reisfeld and Bankoff [21] for the case without aerodynamic loading. Given the nature of the problem, the same assumptions regarding the thin film and the boundary conditions were made here as were made in [13], and so the evolution equation (25) is essentially the same; however, unlike in the previous work, we present (25) in a dimensional rather than non-dimensional format, this being done to facilitate the coupling to the unsteady aerodynamic solver.

Numerical Solver

As the evolution equation (25) is a fourth order, non-linear, non-constant coefficient partial differential equation, it cannot, in general, be solved analytically. Therefore, a pseudo-spectral (or collocation) method solver using an N-point Fourier spectral mode in space and a fourth order Adams–Bashforth time-marching algorithm was constructed. This numerical method was chosen specifically because of the periodic, continuous nature of the problem over the interval [0°, 360°) and the rapid rate of convergence it provides to the solution, given the presumed smoothness of the final result.

As with the mathematical formulation there are again distinct similarities between the present numerical solver and those presented in [13, 21], reflecting the fact that the Fourier pseudo-spectral method is well suited to the problem under examination. The development of the numerical model and the results of a detailed validation and verification study investigating the effects of a static aerodynamic field on the rivulet evolution are presented in [14].

COUPLING AERODYNAMIC AND RIVULET NUMERICAL MODELS

The unsteady aerodynamic solver, and the pseudo-spectral method solver for the water rivulet have been combined to form a coupled solver capable of predicting rivulet formation and evolution subject to an external aerodynamic field which they in turn influence. Experimental studies which consider the evolution of 'natural' rivulets have concentrated on ascertaining the conditions under which RWIV occurs and not on the exact form of these rivulets [5, 6, 8, 9]. Likewise, this is the first time such a solver has been created. Therefore specific data against which to quantitatively verify either the coupled solver, or the results it predicts is unavailable, although qualitative comparison with experimental observations is possible. That said, both of the individual solvers combined to create this coupled solver have been independently validated for related problems [14, 15], which thereby generates a significant level of confidence in the coupled solver.

Construction Of Coupled Solver

A flowchart displaying the basic operation of the coupled solver is displayed in Fig. 3. One inherent aspect of vortex methods, particularly those which employ an operator splitting scheme for the convection and diffusion of the flow, is that "the statistical nature of the results requires the averaging or smoothing of the velocity and pressure distributions and integrated quantities" [20]. Therefore while the mean pressure and shear distributions, $\bar{C}_P$ and $\bar{C}_F$ calculated by DIVEX were smooth, at a specific instant of time there may be significant noise within a given distribution, C_P and C_F. Consequently after interpolating the transient aerodynamic loading determined by DIVEX, such that it can be passed to the thin film solver, this was subjected to smoothing algorithm to reduce any such noise. Further details of the procedure used in the coupling of the two solvers is given in [16].

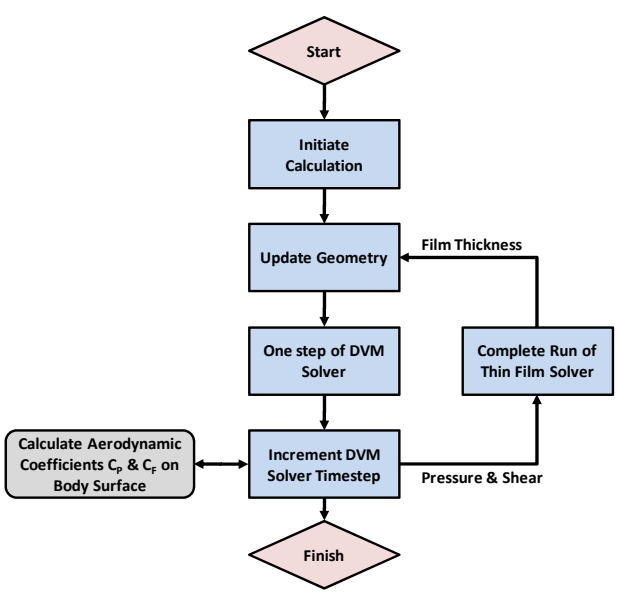

FIGURE 3: SIMPLIFIED FLOWCHART OF THE FINAL COUPLED SOLVER.

Results

The physical parameters used in the study are summarised below in Table 1. The Reynolds number was selected to be 100×10^3, chosen as it represented the mid-point of the typical range for RWIV, $50\times10^3 < \mathrm{Re} < 150 \times 10^3$, as outlined earlier. The cylinder is initially considered to be fully wetted with a film of equal thickness, with an initial film thickness, h_0, of 0.25×10^{-3} m. This particular value being chosen to be consistent with the observations from experiments [5].

TABLE 1. VALUES OF THE STANDARD PARAMETERS USED IN THE NUMERICAL CALCULATION.

Parameter	Value
Cylinder radius, R	0.08 m
Initial film thickness, h_0	2.5×10^{-4} m
Gravity, g	9.806 m/s^2
Density of water, ρ_w	1000 kg/m^3
Dynamic viscosity of water, μ_w	1.002×10^{-3} Ns/m
Surface tension of water, γ	72×10^{-3} N/m
Density of air, ρ	1.19 kg/m^3
Dynamic viscosity of air, μ	1.82×10^{-5} Ns/m

To ascertain whether rivulets do indeed form using distributions of C_P and C_F based upon the evolving cross-section geometry and to determine the differences between these results and those for fixed aerodynamic loading, specifically that of a dry cylinder, four loading combinations were examined. These differed by means of which loads (pressure, shear, surface tension and gravity) were passed between the pseudo-spectral and the aerodynamic solvers and were chosen to match the combinations studied previously [14]. Specifically these were:

1: Shear and surface tension ($P \equiv 0$ and $g = 0$)
2: Pressure and surface tension ($T \equiv 0$ and $g = 0$)
3: Shear, pressure and surface tension ($g = 0$)
4: Full loading (P, T, g and $\gamma \neq 0$)

By choosing these cases the individual effects of shear and pressure loading on coupled rivulet formation could be studied independently, before the combined effect with and without gravitational loading was considered.

Shear and surface tension loading. Figure 4 displays the temporal evolution of film thickness under the combination of shear and surface tension loading. From this three points become apparent. First, as was found previously when this combination of loading was examined for a fixed C_F distribution [14], two larger rivulets formed quickly at approximately the separation points of a dry circular cylinder, one each on the upper and lower surface, with the initial locations of these being $\theta \simeq 83°$ and $\theta \simeq 277°$ on the upper and lower surface respectively. Rivulet location being defined as the point of maximum film thickness clockwise from the windward horizontal θ.

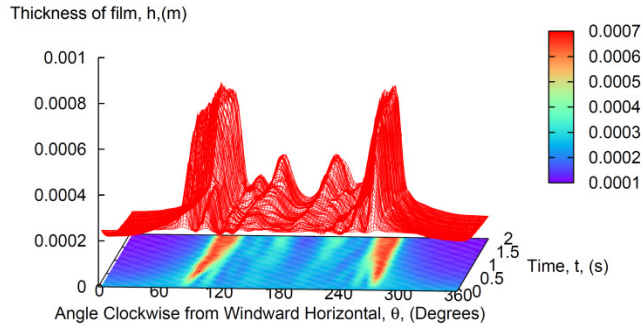

FIGURE 4: NUMERICAL PREDICTION OF TEMPORAL EVOLUTION OF FILM THICKNESS, UNDER SHEAR AND SURFACE TENSION LOADING.

Secondly the growth rate, maximum thickness and form of both the upper and lower of these larger rivulets are approximately equal, (Fig. 5). Even the temporal movement leeward of the points of maximum thickness does so symmetrically with respect to the mean stagnation point of the incident flow, here the windward horizontal (Fig. 6), this leeward progression occurring as the shear load acts tangentially to the surface. As such, once rivulets form they are continually 'pushed' away from the stagnation point of the incident flow, which causes the point of maximum thickness to move from $\theta \simeq 83°$ to $\theta \simeq 93°$ on the upper surface and from $\theta \simeq 277°$ to $\theta \simeq 267°$ on the lower surface. The latter is shown graphically in Fig. 6 in terms of the angle anticlockwise from the windward horizontal θ_{ac} such that the location of the lower rivulet can be directly compared with that of the upper rivulet. Whilst there are small temporal variations in both the thickness and location of the upper and lower rivulets, the evolution of two rivulets can be said to occur in a symmetric manner.

Finally and most importantly, as can be seen from Fig. 5, the maximum thickness of both of the rivulets is self limiting. This is in direct contrast to the previous results [14] when the same combination of loading was examined and where rivulet thickness continued to increase until the thin film approximation was violated. Unlike the previous study however which used a fixed distribution of C_F and that did not account rivulet formation, the distribution of C_F used in the coupled approach does account for the growth of the rivulet and therefore does change with time. As a result the rivulets which develop under an external aerodynamic field they influence grow rapidly to a thickness of $h \simeq 0.65 \times 10^{-3}$ m before remaining of approximately constant thickness. This is a major finding and better reflects the real rivulets of limited thickness which have been found 'in-situ' under RWIV conditions and those which have been found experimentally in the wind-tunnel. The maximum thickness of which, measured experimentally under full loading conditions by Cosentino [5] as $h \simeq 0.55 \times 10^{-3}$ m, is qualitatively in-line with that determined here. The physical mechanism for the rivulet height being self-limiting is complex and has not been completely ascertained. It is felt that once the rivulets reach a certain thickness, an equilibrium state is reached between the aerodynamic loading and the rivulet, whereby the loading does not lead to a change in shape and form of the rivulet. This is still to be confirmed, but the qualitative agreement with experimental observations is again emphasised.

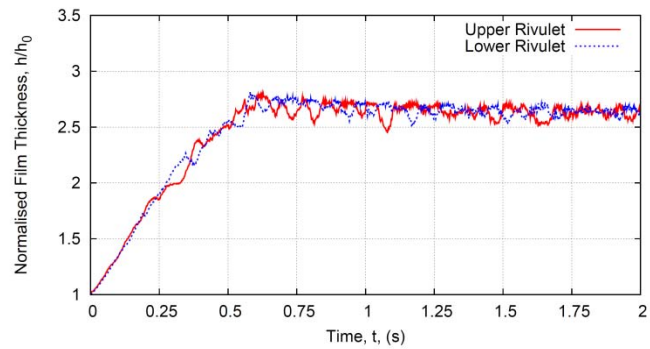

FIGURE 5: TEMPORAL EVOLUTION OF NORMALISED FILM THICKNESS OF UPPER AND LOWER RIVULETS UNDER SHEAR AND SURFACE TENSION LOADING.

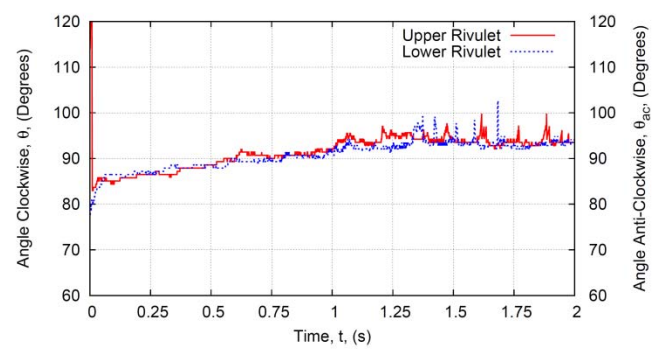

FIGURE 6: TEMPORAL EVOLUTION OF RIVULET LOCATION OF THE UPPER AND LOWER RIVULETS UNDER SHEAR AND SURFACE TENSION LOADING.

Pressure and Surface Tension Loading. The temporal evolution of film thickness for a combination of pressure and surface tension loading can be seen in Fig. 7. This highlights many of the same features of the previous shear loading case. Most notably that two symmetric rivulets of self limiting thickness were found to form marginally windward of the separation points of the dry cylinder, at $\theta \simeq 73°$ and 287° respectively, although two other rivulets were also found in the wake. That said however, the rivulets formed at approximately the separation points under pressure loading were once again found to be located just windward of those formed from shear loading as was determined for evolution due to fixed distributions of C_P and C_F [14]. The second rivulets forming in the wake region are felt to be caused by secondary vortices in the flow due to vortex shedding, and are present in these results due to the coupled nature of the model, where the rivulet shape influences the unsteady pressure distribution and vice versa. This is in contrast to the results in [14], where a fixed pressure distribution was used in the analysis.

Studies into the location, growth rate and thickness of the two rivulets at approximately the separation points of the dry

circular cylinder confirmed that those present on the upper and lower surfaces were once again symmetric images of one another. Figure 8 illustrates the latter two points by comparing the temporal evolution of the upper and lower rivulets' maximum thickness. By comparing this with the temporal evolution of the maximum thickness of the rivulets which form under shear loading (Fig. 5), it can be established that while the magnitude of the rivulets' self limiting thickness are similar, $h \simeq 0.72 \times 10^{-3}$ m from pressure loading as opposed to $h \simeq 0.65 \times 10^{-3}$ m from shear loading, the rates at which these evolve are not. The maximum thickness of the rivulets which evolve due to pressure loading from the external aerodynamic field developing considerably faster than the maximum thickness of those forming due to the shear loading this causes. This is again in good agreement with previous results for fixed pressure and shear distributions [14]. Likewise, the maximum thickness is comparable to experimental results [5].

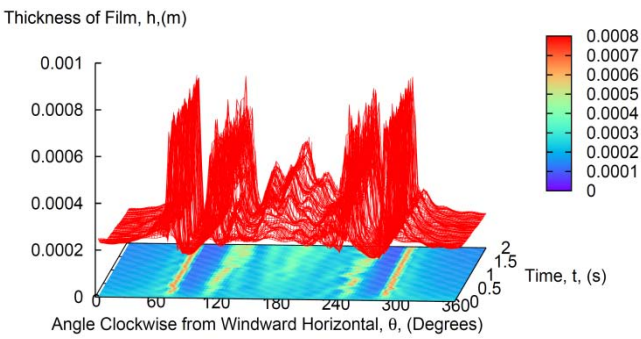

FIGURE 7: NUMERICAL PREDICTION OF TEMPORAL EVOLUTION OF FILM THICKNESS, UNDER PRESSURE AND SURFACE TENSION LOADING.

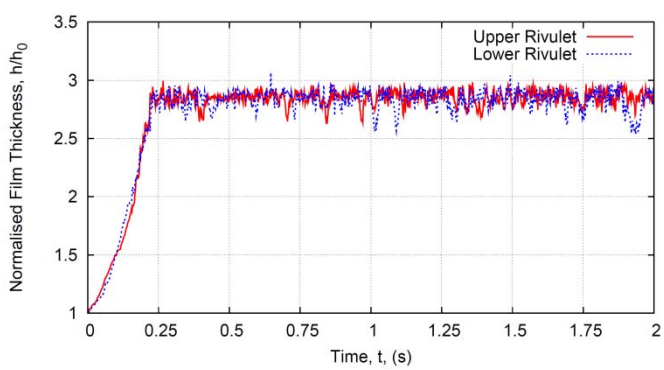

FIGURE 8: TEMPORAL EVOLUTION OF NORMALISED FILM THICKNESS OF UPPER AND LOWER RIVULETS UNDER PRESSURE AND SURFACE TENSION LOADING.

Unlike the shear loading case however while the upper and lower rivulets do form at approximately the same angle from the windward horizontal, clockwise and anti-clockwise respectively, the location of maximum film thickness does not vary significantly with time; remaining approximately constant at $\theta \simeq 73°$. Where because pressure acts normal to the surface, despite some local movement of fluid to allow for the changes in film thickness, there is not the same net flow from the windward to the leeward face that was found in the shear case.

Combined Pressure and Shear Loading. Having studied the effects of both shear and pressure loading separately, a study for both loadings acting in combination with surface tension was undertaken, with the results found to be similar to the previous two independent cases.

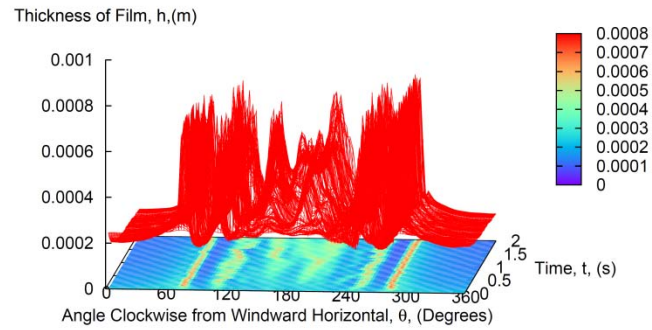

FIGURE 9: NUMERICAL PREDICTION OF TEMPORAL EVOLUTION OF FILM THICKNESS, UNDER PRESSURE, SHEAR AND SURFACE TENSION LOADING.

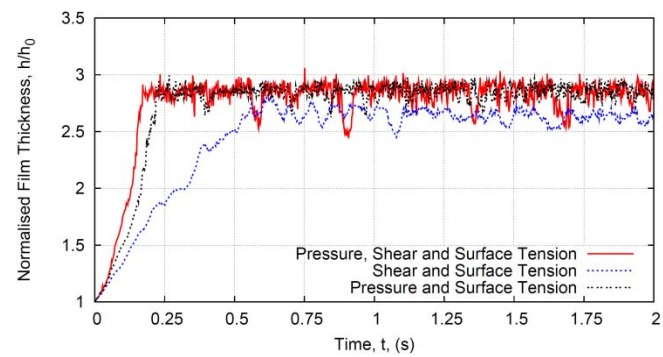

FIGURE 10: COMPARISON OF THE TEMPORAL EVOLUTION OF NORMALISED FILM THICKNESS OF THE UPPER RIVULET FOR VARIOUS LOADING CONDITIONS.

As expected given the symmetry of the rivulets which formed in the individual loading cases, the rivulets which formed under a combination of pressure and shear were again found to be approximately symmetric with respect to the incoming flow (Fig. 9). Furthermore the rivulets formed were once again found to be of self limiting thickness; the maximum magnitudes of which were very similar to the pressure loading case (Fig. 10). The initial growth rate of these rivulets however was marginally quicker than the corresponding growth rate for the independent pressure case as shear loading now works in combination with this to form the rivulet and as such the rivulets under combined loading evolve more quickly. Likewise these rivulets were found to occur at an intermediate location between where the rivulets were found to form in the independent pressure and shear cases (Fig. 11). That said the exact locations of these rivulets at $\theta \simeq 77°$ and $\theta \simeq 283°$, were once again found to be closer to the locations of those formed under only pressure and surface tension loading. These locations of maximum rivulet thickness were also found to remain approximately constant with time, which is also in closer agreement with the pressure loading case than the shear

loading case. Therefore while it can be said that both pressure and shear loading play a role in the evolution of these rivulets, it appears that pressure has greater influence.

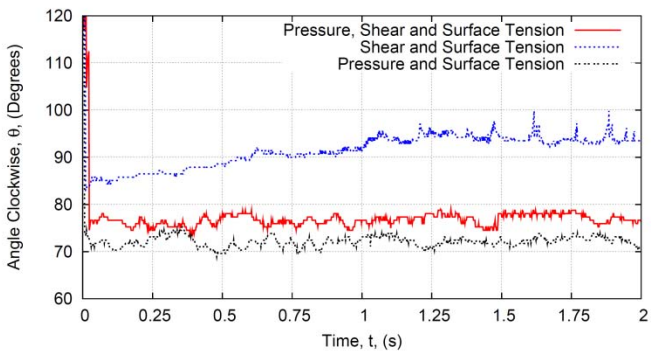

FIGURE 11: COMPARISON OF THE TEMPORAL EVOLUTION OF RIVULET LOCATION OF THE UPPER RIVULET FOR VARIOUS LOADING CONDITIONS.

Full Loading. Given that the coupled solver is two-dimensional and that the governing evolution equation (25) was derived for a horizontal cylinder, the full loading case to be examined here essentially represents the physical loading on a horizontal cable perpendicular to the incoming flow, i.e. $\alpha = \beta = 0°$ (Fig. 1). In comparison with the previous loading combinations, there are significant differences in the variation of film thickness for the present case (Fig. 12).

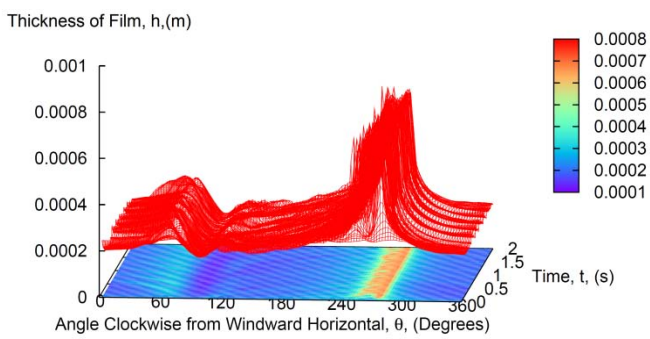

FIGURE 12: NUMERICAL PREDICTION OF TEMPORAL EVOLUTION OF FILM THICKNESS, UNDER FULL LOADING.

The most noticeable of these differences being that, as expected, the symmetry of the three previous cases examined is lost due to the effect of gravity. The 'noise' present when pressure loading was considered either individually or in combination with the shear loading is also considerably lessened. In combination with the lack of symmetry, this indicates that gravity has a stronger influence than either of the loadings due to the external aerodynamic field (pressure and shear) for the present conditions, although these do still play a role. Therefore while a distinct rivulet can be seen to form on the lower surface at approximately the lowest point on the cylinder, $\theta \simeq 277°$, the temporal evolution of the upper surface is more complicated and necessitates more detailed review. These two surfaces are therefore discussed separately.

The thickness of this lower rivulet, like those of the previous loading cases investigated, is self limiting. In this instance at approximately 0.68×10^{-3} m, which is consistent with previous results and is quantitatively in-line with the upper rivulet measured experimentally [5]. Furthermore as this rivulet forms on the lower surface, due to the additional effect of gravity this evolves more quickly than any of the previous loading combinations examined. The location of this rivulet as defined by the point of maximum thickness has likewise moved leeward (towards the lowest point) from the combined shear and pressure case due to the effect of gravity.

While the lower rivulet is easy to distinguish, the evolution of the thin film on the upper surface is considerably more complicated. A small rivulet does periodically form on the upper surface at approximately $\theta = 67°$ (Fig. 12), before moving away in a 'rippling' motion due to the combination of aerodynamic and gravitational loading. The thickness and location of this rivulet therefore vary with time. Figure 13 illustrates this periodic formation of rivulets by tracking the variation in film thickness at $\theta = 67°$, from which the period of formation can also be determined as approximately 0.23 s. Interestingly this is three times the period of Karman vortex shedding for this body, which is the same value that was found by Matsumoto [3] to play an important role in a high reduced velocity vortex-induced vibration (HSV) phenomenon. As such the periodic appearance of this rivulet at an angular location which has already been determined to have a major impact on the flow via the artificial rivulets studies [15, 19] and previous experimental studies [7-9], may prove to be a contributory factor to the underlying cause of the HSV phenomenon and explain why a frequency of $\frac{1}{3}f_s$ is so important to this. This however is only an initial observation and as the axial vortex previously identified [3] as being of central importance to this is a three-dimensional flow feature, it cannot be captured in the present work, as such this conjectured link is very tentative. Further work to investigate any such link is a subject of future research projects.

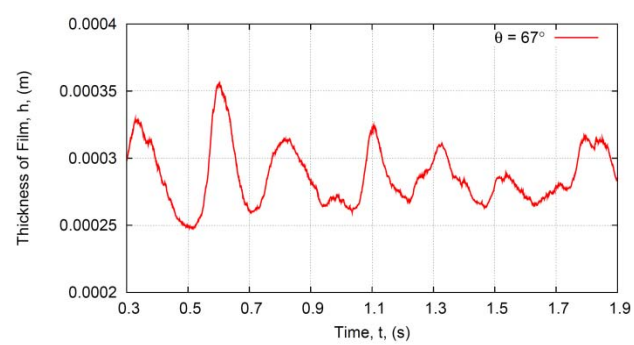

FIGURE 13: TEMPORAL EVOLUTION OF FILM THICKNESS AT A LOCATION 67° CLOCKWISE FROM THE WINDWARD HORIZONTAL UNDER FULL LOADING CONDITIONS.

As can be seen from Fig. 14 which is a magnified version of the area of interest of the overall film surface evolution (Fig. 12), the 'rippling' motion originates in two locations each moving in a different direction before joining the larger lower

rivulet. Although smaller ripples develop downstream of the separation point of a dry cylinder and move in a leeward direction, they are within the wake and so have little effect on the flow. The rivulets on the upper surface form in the region previously determined to be danger for RWIV, $\theta = 67°$ [15, 20], and move in a windward direction. The motion of the rivulets on the surface, also qualitatively match the observations of moving rivulets in experiments [4, 7].

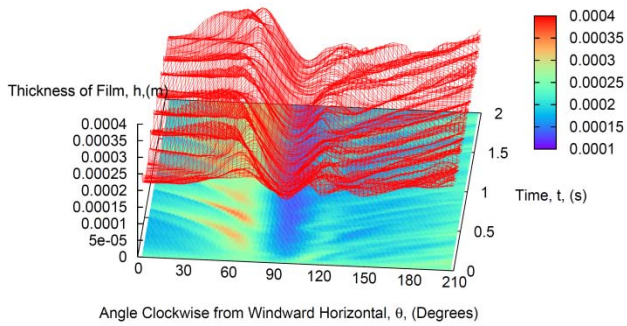

FIGURE 14: NUMERICAL PREDICTION OF TEMPORAL EVOLUTION OF FILM THICKNESS, UNDER FULL LOADING OF REGION NEAR THE UPPER RIVULET.

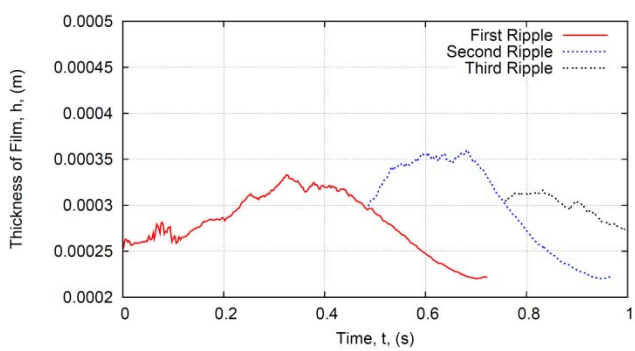

FIGURE 15: TEMPORAL EVOLUTION OF MAXIMUM THICKNESS OF INDIVIDUAL RIPPLES ON THE UPPER SURFACE, UNDER FULL LOADING CONDITIONS.

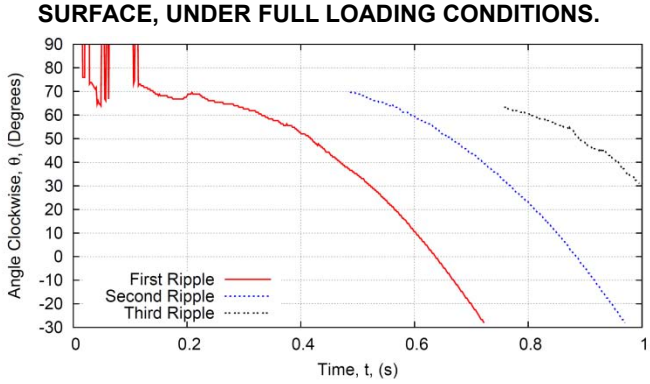

FIGURE 16: TEMPORAL EVOLUTION OF INDIVIDUAL RIPPLE LOCATION CLOCKWISE FROM THE WINDWARD HORIZONTAL, UNDER FULL LOADING CONDITIONS.

Figures 15 and 16 track the magnitude and location of the point of maximum thickness for each of these 'ripples' for the first second of evolution studied. These illustrate that after an initial transient period of approximately 0.2 s where the whole film is evolving that the formation and movement of these 'ripples' is approximately periodic. The extent of the initial transient period corresponds well with the time for the thickness of lower rivulet to reach the self limiting thickness. A new rivulet evolves approximately every 0.23 s at $\theta \simeq 67°$, before beginning to move windward under the effect of gravity. These rivulets increase in thickness until $\theta \simeq 50°$ where they begin to 'spread', decreasing in thickness and increasing in circumferential velocity until joining the lower rivulet approximately 0.6 s later. Given that the thickness of both the lower rivulet and the mean surface do not vary after the initial formation period, it can be surmised that there is no net movement of fluid during this rippling process. Rather individual points on the film surface rise and fall in a manner similar to ocean waves. It should also be noted that the initial location and the thickness of the rivulet are consistent with the previous cases and with experimental observations [5].

CONCLUSIONS

A coupled model to investigate the Rain-Wind-Induced Vibration of cables has been developed, which utilizes an unsteady aerodynamic solver together with a pseudo-spectral model to solve the evolution equation, for the water rivulet. This novel approach provides the most detailed simulations of the RWIV phenomenon to date.

Four combinations of loading were investigated, to examine the independent effects of shear and pressure, before combining these and finally adding gravity to ascertain the effects of the full physical loading on the rivulet dynamics.

The location and growth rates of the rivulets formed in each case agree well with previous investigations using fixed aerodynamic loading and with each other. These were located marginally windward of the separation points of the dry cable and symmetric with respect to the incident flow when gravity was not considered.

For the first time the thickness of the rivulets were found to be self limiting as a result of varying aerodynamic load due to rivulet growth. The thickness of the rivulets was found to be in excellent agreement experimental results.

When gravitational loading was considered, this symmetry was lost with a larger lower rivulet found to evolve with approximately the same growth rate and the thickness as those under previous loading conditions. This was once again of self-limiting thickness. On the upper surface a rivulet was only found to form periodically, before moving to join the lower rivulet, with this periodic nature being consistent with previously identified key mechanisms for RWIV.

ACKNOWLEDGMENTS

Andrew Robertson, gratefully acknowledges the support of the UK Engineering and Physical Sciences Research Council (EPSRC) via a Doctoral Training Account studentships. The support of Prof. Stephen Wilson, Dr Brian Duffy and Dr Julie Sullivan, Department of Mathematics, University of Strathclyde, in deriving the evolution equation is gratefully acknowledged.

NOMENCLATURE

B	solid body in unsteady aerodynamic solver
$\bar{C}_F$, $\bar{C}_P$	mean (time averaged) coefficient of friction / pressure
C_F, C_P	coefficient of friction / pressure
D	Diameter of cable
F	flow field in unsteady aerodynamic solver
H, h	thickness of water film on surface of cylinder
i, j, k	unit orthogonal vectors
$\boldsymbol{n}$, n	unit vector and distance normal to body surface
P	pressure distribution
Q	azimuthal volume flux of fluid in the film
Re	Reynolds number $= U_\infty D/\nu$
r	position vector
r, θ, z	polar coordinates : z axis along the axis of the cylinder, θ measured from upstream stagnation point
$\boldsymbol{s}$, s	unit vector and distance tangential to body surface
S	surface of body in unsteady aerodynamic solver
T	shear distribution
t	time
$\mathbf{U}$, U	velocity vector and magnitude
u, v	horizontal and vertical velocities
x, y	horizontal and vertical directions
α	cable inclination angle
β	cable yaw angle (angle of cable to wind direction)
γ	surface tension of water
ε	ratio of thickness of film to cylinder radius ($= H/R$)
ζ	damping ratio
θ	angle around circumference of cylinder
κ	mean curvature of the free surface of the film
μ	dynamic viscosity of fluid
ν	kinematic viscosity of fluid
ρ	density of fluid
$\boldsymbol{\Psi}$, Ψ	vector potential and stream function
Ω	rotational velocity of solid body
$\boldsymbol{\omega}$, ω	vorticity (vector and magnitude)

REFERENCES

[1] Hikami, Y., and Shiraishi, N., 1988, "Rain-Wind Induced Vibrations of Cables in Cable Stayed Bridges," Jl. Wind Eng. Ind. Aero., **29**(1-3), pp. 409-418.

[2] Zuo, D., Jones, N.P., and Main, J.A., 2008, "Field Observation of Vortex- and Rain-Wind-Induced Stay-Cable Vibrations in a Three-Dimensional Environment," Jl. Wind Eng. Ind. Aero., **96**(6-7), pp. 1124-1133.

[3] Matsumoto, M., Yagi, T., Shigemura, Y., and Tsushima, D., 2001, "Vortex-Induced Cable Vibration of Cable-Stayed Bridges at High Reduced Wind Velocity," Jl. Wind Eng. Ind. Aero. **89**(7-8), pp. 633-647.

[4] Wang, Z.J., Zhou, Y., Huang, J.F., and Xu, Y.L., 2005, "Fluid Dynamics Around an Inclined Cylinder with Running Water Rivulets," Jl. Fluids Struc., **21**(1), pp. 49-64.

[5] Cosentino, N., Flamand, O., and Ceccoli, C., 2003, "Rain-Wind Induced Vibration of Inclined Stay Cables. Part I: Experimental Investigation and Physical Explanation," Wind and Structures, **6**(6), pp. 471-484.

[6] Verwiebe, C., and Ruscheweyh, H., 1998, "Recent Research Results Concerning the Exciting Mechanism of Rain-Wind-Induced Vibrations," Jl. Wind Eng. Ind. Aero., **74-76**, pp. 1005-1013.

[7] Bosdogianni, A., and Olivari, D., 1996, "Wind and Rain Induced Oscillations of Cables of Stayed Bridges," Jl. Wind Eng. Ind. Aero. **64**(2-3), pp. 171-185.

[8] Gu, M., and Du, X., 2005, "Experimental Investigation of Rain-Wind-Induced Vibration of Cables in Cable Stayed Bridges and its Mitigation," Jl. Wind Eng. Ind. Aero., **93**(1), pp. 79-95.

[9] Flamand, O., 1995, "Rain-Wind Induced Vibration of Cables," Jl. Wind Eng. Ind. Aero., **57**(2-3), pp. 353-362.

[10] Gu, M., and Huang, L., 2008, "Theoretical and Experimental Studies on the Aerodynamic Instability of a Two-Dimensional Circular Cylinder with a Moving Attachment," Jl. Fluids Struc., **24**(2), pp. 200-211.

[11] Matsumoto, M., Shiraishi, N., and Shirato, H., 1992, "Rain-Wind Induced Vibration of Cables of Cable-Stayed Bridges," Jl. Wind Eng. Ind. Aero., **41-44**, pp. 2011-2022.

[12] Li, S.Y., and Gu, M., 2006, "Numerical Simulations of Flow Around Stay Cables With and Without Fixed Artificial Rivulets," Proc. 4th Int. Symp. Comp. Wind Eng. (CWE2006), Yokohama, Japan, pp. 307-310.

[13] Lemaitre, C., Hemon, P., and De Langre, E., 2007, "Thin Water Film Around a Cable Subject to Wind," Jl. Wind Eng. Ind. Aero., **95**(9-11), pp. 1259-1271.

[14] Robertson, A.C., Taylor, I.J., Wilson, S.K., Duffy, B.R., and Sullivan, J.M., 2010, "Numerical Simulation of Rivulet Evolution on a Horizontal Cable Subject to an External Aerodynamic Field," Jl. Fluids Struc., **26**(1), pp. 50-73.

[15] Taylor, I.J, Robertson, A.C., Wilson, S.K., Duffy, B.R., and Sullivan, J.M., 2010, "Recent Developments in Rain-Wind Induced Vibrations of Cables," Proc. Inst. Civil Eng. : Struc. And Bldgs., **163**(SB2), pp. 73-86.

[16] Robertson, A.C., 2009, "Numerical Simulation of Rivulet Dynamics Associated with Rain-Wind Induced Vibration," Ph.D. Thesis, Dept. of Mechanical Engineering, University of Strathclyde, Glasgow, Scotland, UK.

[17] Taylor, I.J., and Vezza, M., 1999, "Prediction of Unsteady Flow Around Square and Rectangular Cylinders using a Discrete Vortex Method," Jl. Wind Eng. Ind. Aero., **82**(1-3), pp. 247-269.

[18] Taylor, I.J., and Vezza, M., 2001, "Application of a Discrete Vortex Method for the Analysis of Suspension Bridge Deck Sections," Wind and Structures, **4**(4), pp. 333-352.

[19] Matsumoto, M., Yagi, T., Adachi, Y., Hatsuda, H., and Shima, T., 2007, "Karman Vortex Effects on Aerodynamic Instabilities of Inclined Stay-Cables," Proc. 12th Int. Conf. Wind Eng. Cairns, Australia, pp. 175–182.

[20] Sarpkaya, T., 1989, "Computational Methods with Vortices - The 1988 Freeman Scholar Lecture," Jl. Fluids Eng., **111**(1), pp. 5-52.

[21] Reisfeld, B., and Bankoff, S.G., 1992, "Non-Isothermal Flow of a Liquid Film on a Horizontal Cylinder," Jl. Fluid Mech., **236**, pp. 167-196.